Chapter 2

Background

In this chapter, the experimental systems and the theoretical framework of the present work are described. To begin with, some basic concepts of reaction-diffusion systems are recalled. In the second part, the catalytic oxidation of CO on Pt(110) is introduced as a paradigmatic model system for nonlinear catalytic surface reactions and reaction-diffusion systems in general. Furthermore, an example of a reaction-migration system, the electrochemical oxidation of hydrogen on Pt, is discussed. Finally, general models are presented that allow the study of generic aspects common to many extended dynamical systems.

2.1 Reaction-diffusion systems

In many cases, the spontaneous emergence of spatiotemporal patterns in extended systems far from thermodynamic equilibrium can be understood as an interplay between local dynamics of individual system elements and coupling of these elements. In the large class of reaction-diffusion systems, coupling occurs due to diffusive transport induced by differences in the states of neighboring elements. Although the present section is focused on systems with diffusive coupling, it is pointed out that other coupling mechanisms may occur like global coupling or migrational coupling, as will be discussed later.

2.1.1 Homogeneous dynamics

Suppose that the state of a single active element can be expressed in terms of a set of time-dependent variables $\mathbf{u} = (u_1, u_2, \dots, u_n)$. The temporal behavior of the element can be generally described by a set of n coupled ordinary differential equations,

$$\dot{\mathbf{u}} = \mathbf{f}(\mathbf{u}, \mathbf{p}), \tag{2.1}$$

with functions $\mathbf{f}(\mathbf{u}, \mathbf{p})$ that depend on a number of parameters $\mathbf{p} = (p_1, p_2, \dots, p_m)$. Our interest here is focused on chemical systems, where the variables $\mathbf{u}$ mostly denote concentrations of reacting species and the functions $\mathbf{f}$ represent the kinetics of the reaction, depending on parameters such as rate constants and external conditions. The case of Eq. (2.1) is often referred to as the *homogeneous dynamics* since it describes the situation of a well stirred reactor. Mixing ensures a uniform distribution of reactants so that diffusive transport is absent.

Although in many cases the set of Eqs. (2.1) is of low dimension, the temporal dynamics can be complex, in particular, if the functions $\mathbf{f}$ involve nonlinear terms. In the following paragraphs, basic ideas of the theory of low-dimensional dynamical systems are briefly introduced. For a more thorough treatment the reader is referred to standard introductory textbooks [20, 21].

Phase space Each state of a dynamical system (2.1) corresponds to a point in *phase space* which is spanned by the variables $u_1, u_2, \dots, u_n$. Trajectories in phase space, so-called *orbits*, represent the temporal evolution of the system starting from an initial condition $\mathbf{u_0}$. The dynamics is *deterministic* since each future and past state of the system is uniquely determined by the functions $\mathbf{f}$ for any given initial condition. The temporal behavior of the system is governed by the topology of its phase space. The phase space may, for instance, show regions where trajectories get trapped. Any trajectory that starts within such an *invariant set* remains there forever. Some invariant sets may be attracting so that trajectories from their neighborhood approach the invariant set for $t \to \infty$. They are referred to as *attractors* sitting within their *basin of attraction*. Invariant sets can correspond to stationary states (see the following paragraph) or *limit cycles* upon which trajectories are periodic. In more complex cases, they may be quasi-periodic or chaotic.

Fixed points and stability Stationary invariant sets $\mathbf{u^s}$ are called *fixed points*. They are defined by the condition $\dot{\mathbf{u}} = 0$. When discussing fixed points, the question of stability becomes a key issue for understanding the dynamics and for classifying different kinds of fixed points. Most commonly, stability is studied with respect to a small perturbation $\delta\mathbf{u}(t) \equiv \mathbf{u}(t) - \mathbf{u^s}$ in a *linear stability analysis*. Equation (2.1) is linearized around the fixed point $\mathbf{u^s}$ by a Taylor expansion up to the linear term, thus yielding

$$\dot{\delta\mathbf{u}} = \mathbf{J}(\mathbf{u^s})\,\delta\mathbf{u} \qquad \text{with} \qquad J_{ij} = \frac{\partial f_i}{\partial u_j}\,. \tag{2.2}$$

The real parts of the eigenvalues $\lambda_1, \lambda_2, \ldots, \lambda_n$ of the Jacobian $\mathbf{J}$ at the fixed point $\mathbf{u^s}$ are the exponential growth rates of the perturbation $\delta\mathbf{u}$ along the eigenvectors of $\mathbf{J}$ and, therefore, determine the stability of $\mathbf{u^s}$. The fixed point is stable if $\mathrm{Re}\,\lambda_i < 0$ for all $i = 1, 2, \ldots, n$. If the real part of at least one eigenvalue is positive, $\mathbf{u^s}$ is unstable. For a two-dimensional phase space the pair of eigenvalues is given by the solution of a

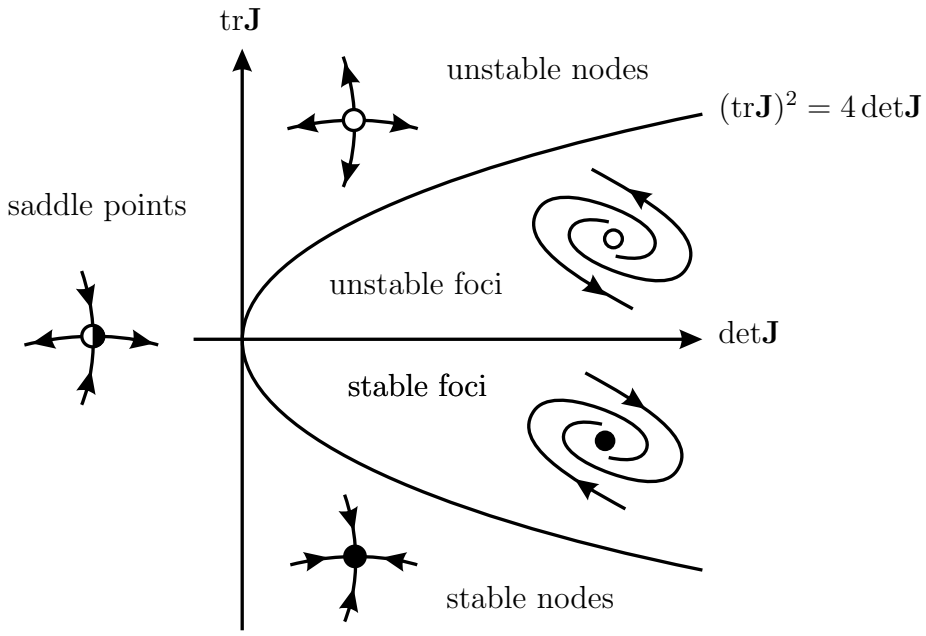

Figure 2.1: Fixed points in two-dimensional vector fields. Type and stability of a fixed point is determined by the eigenvalues of the Jacobian $\mathbf{J}$. The line $\mathrm{det}\mathbf{J} = 0$ separates saddles from nodes and the curve $(\mathrm{tr}\mathbf{J})^2 = 4\ \mathrm{det}\mathbf{J}$ nodes from foci.

quadratic equation,

$$\lambda_{1,2} = \frac{1}{2}\left(\mathrm{tr}\mathbf{J} \pm \sqrt{(\mathrm{tr}\mathbf{J})^2 - 4\,\mathrm{det}\mathbf{J}}\right) , \tag{2.3}$$

where tr$\mathbf{J}$ and det$\mathbf{J}$ denote the trace and the determinant of the Jacobian $\mathbf{J}$, respectively. Thus, the eigenvalues are either real or complex conjugate. If the eigenvalues are real and positive (negative) they indicate an unstable (stable) node, while the combination of both a positive and a negative eigenvalue corresponds to a saddle point. For complex conjugate eigenvalues a stable or unstable focus is found depending on the sign of the real parts of $\lambda_{1,2}$. The different types of fixed points for a two-dimensional vector field are summarized in Fig. 2.1.

In addition to fixed points, where the temporal derivative of all dynamical variables becomes zero, other elements in phase space can be considered to understand the dynamics of a system (2.1). In particular, it is helpful to analyze the *nullclines* of a system. They are defined by $\dot{u}_i = 0$, *i.e.*, depending on the dimension of the system, they represent curves, planes, or hyper-surfaces in phase space, on which the temporal derivative of one of the dynamical variables is zero. Fixed points correspond to locations, where all nullclines intersect. As will be seen later, nullclines are particularly useful to analyze the behavior of two-dimensional systems.

Bifurcations The topological structure of trajectories in phase space depends on the choice of the parameters $\mathbf{p}$ in the functions $\mathbf{f}$ on the right hand side of Eq. (2.1). If the parameters are varied, qualitative changes in the topology may occur at distinct critical values $\mathbf{p_c}$. These changes are called *bifurcations* and the corresponding points $\mathbf{p_c}$ in parameter space are *bifurcation points*. For example, fixed points can emerge or disappear in a bifurcation or their stability may change. Consider, for instance, the simple one-dimensional system

$$\dot{u} = pu - u^3 . \tag{2.4}$$

There is one fixed point at $u_1 = 0$ for $p < 0$. If the parameter p is increased, a bifurcation occurs for $p_c = 0$ and two new fixed points emerge at $u_{2,3} = \pm\sqrt{p}$. Linear stability analysis shows that these new fixed points are stable, while the fixed point u_1 is stable only for negative p and loses its stability beyond the bifurcation point. This

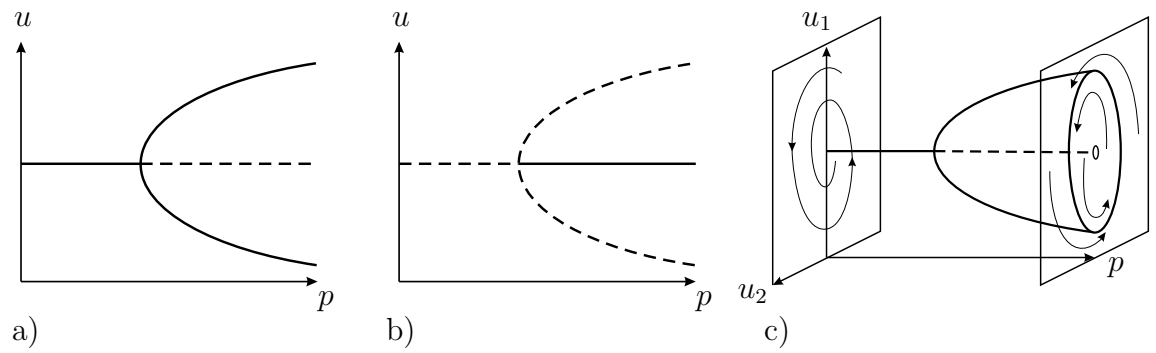

Figure 2.2: (a) Supercritical pitchfork bifurcation, (b) subcritical pitchfork bifurcation, and (c) supercritical Hopf bifurcation. The variables are denoted by u_1 and u_2, the control parameter by p. Solid (dashed) lines correspond to stable (unstable) states.

scenario is denoted as a *pitchfork bifurcation* and can be illustrated in a *bifurcation diagram* as shown in Fig. 2.2 (a). In the context of this work, the simplest example of a bifurcation that leads to oscillatory behavior is of particular interest. In a *Hopf bifurcation*, a stable focus becomes unstable upon change of an appropriate control parameter and gives rise to a stable limit cycle as shown in Fig. 2.2 (c). Close to the bifurcation point, the oscillations are harmonic and their amplitude shows a square root dependence on the distance from the bifurcation point.

Some bifurcations may appear in a super- or a subcritical form. In a *supercritical* bifurcation, existing solutions become unstable and newly emerging solutions are stable while for a *subcritical* bifurcation the opposite is true. This distinction is also relevant for the above explained pitchfork and the Hopf bifurcations. They were both introduced in their supercritical form. As an example for a subcritical bifurcation, see the subcritical pitchfork bifurcation in Fig. 2.2 (b).

2.1.2 Extended Systems

Let us consider a spatially extended system composed of a large number of coupled identical active elements that show deterministic dynamics according to Eq. (2.1). In addition to time-dependence, the variables $u_1, u_2, \ldots, u_n$ now also depend on spatial coordinates. In the limit of a continuous medium and for diffusive coupling, the dynamics of such a system will in general be described by Eq. (2.1) with an additional diffusive

coupling term. We thus consider n coupled nonlinear partial differential equations of reaction-diffusion type for the variables u_i,

$$\partial_t \mathbf{u} = \mathbf{f}(\mathbf{u}\,, \mathbf{p}) + \mathbf{D}\nabla^2\,\mathbf{u}\,. \tag{2.5}$$

In agreement with Eq. (2.1), the set of functions $\mathbf{f}(\mathbf{u}, \mathbf{p})$ accounts for the local dynamics depending on parameters $\mathbf{p}$. The diffusion matrix $\mathbf{D}$ often takes diagonal form if diffusion of the different species can be considered independently of each other. In the context of chemical reaction-diffusion systems, Eq. (2.5) can be regarded as a model for an unstirred reactor, where concentrations may vary between different locations inducing diffusive fluxes. However, it is stressed that besides chemical reactions, Eq. (2.5) may describe systems of quite different origin from a large range of disciplines like physics, environmental sciences, and cellular biology [25].

Spatially extended systems are commonly classified according to the local dynamics of their individual elements. In this way, many systems of form (2.5) can be assigned to one of a few overall categories of temporal behavior. In many cases, their dynamics is either monostable, bistable, excitable, or oscillatory [25]. In the trivial case of a *monostable* system the dynamics is determined by a single stable fixed point. Under perturbations, the system will experience damping and always returns to the same stable steady state.

Bistable systems The behavior of a bistable system is characterized by the presence of two stable steady states. For small perturbations the system remains in one of the stable states, while under sufficiently strong perturbations transitions between the two states may occur. For a two-dimensional bistable system the nullclines generally show three intersection points as depicted in Fig. 2.3 (a). Two of them are stable fixed points corresponding to the two stable steady states. In between lies a saddle point separating the two stable states. The shapes of the basins of attraction of the two fixed points depend on the characteristic time scales of the two variables. In a spatially extended bistable system, a local transition between the two stable steady states can induce a similar switching of the neighboring elements so that the transition starts to spread in a *trigger wave* through the medium. Trigger waves are the basic patterns in bistable systems. Their propagation velocity is uniquely determined by the properties of the medium.

Excitable systems As in the monostable case, excitable systems exhibit only one stable fixed point corresponding to a single intersection of the nullclines in phase space, see Fig. 2.3 (b). However, assuming that the dynamics of the variable u_1 is fast compared to u_2, the situation is more complicated here. While small perturbations applied to the stationary state decay rapidly back to the stable fixed point, larger perturbations exceeding a certain threshold induce a more complex response of the system. The excitation barrier for this behavior is determined by the repelling middle branch of the nullcline $\dot{u}_1 = 0$. Once a sufficiently large perturbation has driven the system across this barrier, it is attracted by the stable right branch of the $\dot{u}_1 = 0$ nullcline and performs an extended excursion through phase space back to the stable fixed point. This is indicated in Fig. 2.3 (b). The characteristic time needed to recover from an excitation is called the *refractory period* of the system.

In an extended system with sufficiently strong diffusive coupling, an excitation can spread through the medium, forming a propagating excitation pulse. Since each element returns to its initial state after the excitation has passed, traveling pulses can repeatedly pass through the same location. This enables the formation of more complex spatiotemporal patterns compared to bistable systems. Upon collision, excitation pulses mutually annihilate; if they break, their ends start to curl and form rotating spiral waves with a characteristic wavelength and rotation frequency that depend on the system properties only. Upon a change of parameters, spiral waves may undergo different instabilities leading to more complex dynamics like drift motion, complicated

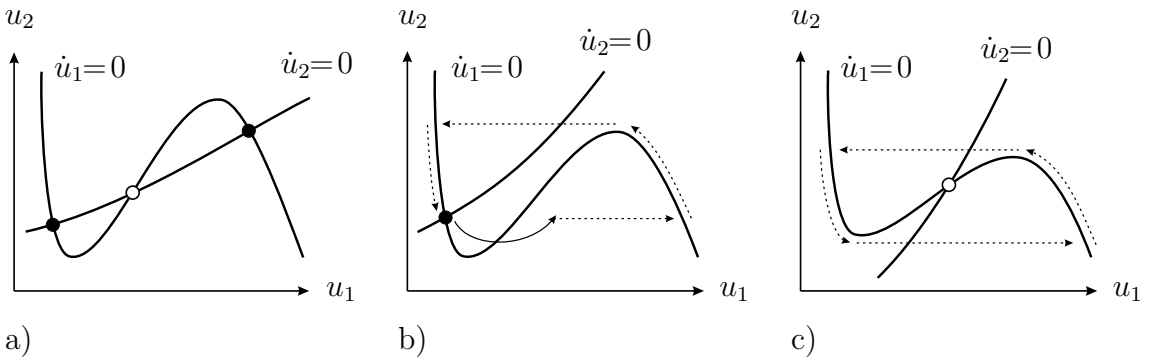

Figure 2.3: Schematic phase space diagrams showing nullclines and fixed points of (a) a bistable, (b) an excitable, and (c) an oscillatory system. Trajectories in phase space (dotted lines) are displayed assuming a clear separation of time scales (u_1 has fast dynamics compared to u_2).

meandering of spiral centers [83,84], or a transition to chemical turbulence via breakup of spiral waves [85].

Oscillatory systems The phase space of a self-sustained oscillator typically shows the combination of an unstable fixed point and a stable limit cycle. In the two-dimensional case of Fig. 2.3 (c), the unstable steady state corresponds to the intersection point of the nullclines on the unstable middle branch of the nullcline $\dot{u}_1 = 0$. The limit cycle oscillations are indicated by dotted arrows for the case of a fast variable u_1 and a slow variable u_2. In the simplest case, the limit cycle is the only attractor in phase space so that the system cannot settle down to a stationary configuration. For any initial condition, it eventually ends up on the limit cycle and remains there.

A spatially extended oscillatory system can be regarded as the continuous limit of a large coupled population of such oscillating elements. Most of the present work will be concerned with oscillatory systems that show a rich variety of spatiotemporal pattern formation phenomena. Simple plane waves are found if a constant phase gradient is maintained along some direction through the system. As in excitable systems, also spiral and target waves can be observed. Target patterns are formed by concentric waves that are periodically emitted from a small central region called pacemaker. Although stable target patterns can already form in uniform reaction-diffusion systems resulting from the combination of nonlinear kinetics and diffusion [86], the majority of target patterns in chemical systems is associated with the presence of local heterogeneities, see *e.g.* Ref. [87] and references therein. If oscillations desynchronize in the course of time a turbulent regime is established in the system. This situation typically occurs when diffusive coupling destabilizes uniform oscillations by amplifying existing phase gradients.

The local oscillations can be characterized in terms of oscillation phase and amplitude variables. If the phase varies smoothly across the system, the distribution of phases will evolve on a time scale which is large compared to the characteristic amplitude relaxation time of the individual oscillators. Under this condition, the amplitude adjusts adiabatically to the local phase gradient and the dynamics can be described in terms of the phase variable only. The corresponding phase dynamics equation universally describes the evolution of smooth phase distributions in any oscillatory system, see also Section 2.4.2.

2.2 The catalytic CO oxidation on Pt(110)

In the previous section, basic concepts of nonlinear dynamics and pattern formation in reaction-diffusion systems were summarized. We now turn to a specific reaction-diffusion system, the catalytic oxidation of CO on Pt(110), that will serve as a model system for both experimental and theoretical studies throughout this work. The catalytic CO oxidation on platinum is one of the most thoroughly studied heterogeneous catalytic surface reactions [47]. It shows, among other nonlinear surface reactions, a particularly rich dynamics including a large variety of spatiotemporal phenomena [45].

2.2.1 Pattern formation in the CO oxidation system

Before describing the kinetics and the microscopic mechanism of catalytic CO oxidation on Pt(110), typical phenomena of nonlinear kinetics and spatiotemporal self-organization in this reaction will be reviewed.

The first observations of oscillatory kinetics in heterogeneous catalysis go back to Wicke and coworkers, who reported oscillating reaction rates for the catalytic oxidation of CO in the beginning of the 1970s [88, 89]. Besides CO oxidation, many other cases of oscillatory heterogeneous catalytic reactions were observed in the last thirty years, among them the oxidation of hydrocarbons, the reduction of NO, and the oxidation of hydrogen, to mention only a few of them. For a review the reader is referred to [45].

Early studies of oscillating surface reactions were typically performed under rather high pressures and on poorly defined surfaces. To obtain a more detailed insight into the mechanism responsible for rate oscillations in heterogeneous reactions, investigations were focused on processes at well-defined single crystal surfaces under low pressure conditions. In 1982, Ertl and coworkers reported oscillatory kinetics for the oxidation of CO on Pt(100) [90] and in 1986 for CO oxidation on Pt(110) [91], where rich temporal dynamics could be observed including period doubling and deterministic chaos [92].

With the development of novel imaging techniques in the 1990s, investigations were no longer restricted to temporal behavior and the observation of spatiotemporal phenomena during catalytic reactions at single crystal surfaces became possible. The first spa-

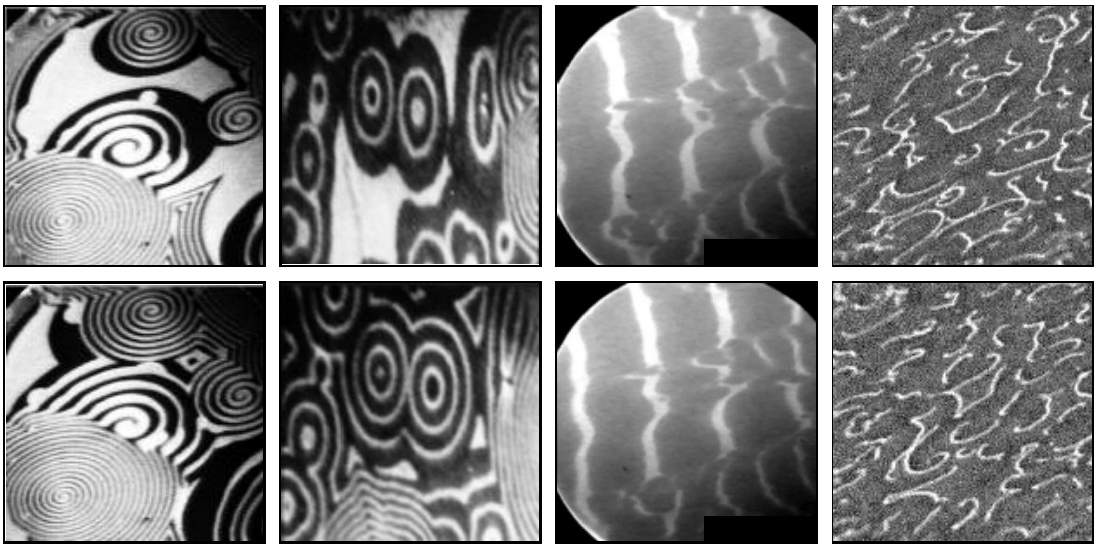

Figure 2.4: Images of typical patterns during CO oxidation on Pt(110) obtained by photoemission electron microscopy (PEEM). Dark areas correspond to mainly oxygen covered regions and bright areas are mostly CO covered. (a) Rotating spiral waves [93], (b) target patterns [46], (c) standing waves [94], and (d) chemical turbulence [95]. Two subsequent snapshots of each pattern are shown (top and bottom row).

tially resolved real time images of concentration patterns on a catalyst surface were obtained by photoemission electron microscopy (PEEM, for details see Section 2.2.5) [96]. Later, also optical methods were established [94]. Ellipsomicroscopy for surface imaging (EMSI) and reflection anisotropy microscopy (RAM) allow the observation of self-organization on the catalyst surface even at high pressures [97, 98].

Typical spatiotemporal patterns observed during catalytic CO oxidation on Pt(110) under low pressure conditions ($p < 10^{-3}$ mbar) are solitary waves and pulses, rotating spiral waves, target patterns, standing waves, and chemical turbulence [46, 93, 99]. Examples are displayed in Fig. 2.4 (note that curved patterns are elliptically elongated due to anisotropy of CO diffusion on the Pt(110) surface, as will be explained below). In later studies, pattern formation on microdesigned composite catalysts was investigated exploring self-organization in confined domains and interactions of patterns with active boundaries [58, 59, 100]. More recently, efforts were made to guide the processes of self-assembly on the catalyst at will. A new approach was developed to locally influence and control the spatiotemporal dynamics during CO oxidation using a focused laser beam [60, 101–103].

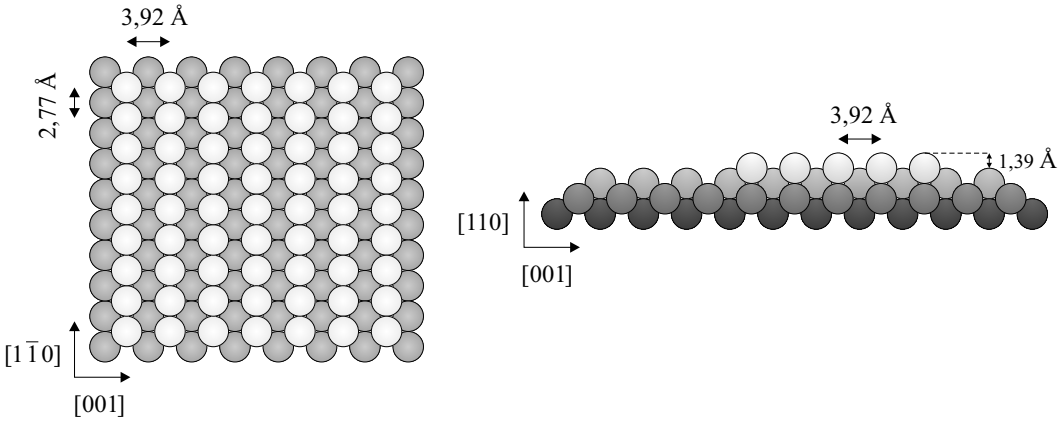

Figure 2.5: Hard-sphere model showing the (1×1) structure of the Pt(110) surface. Top view (left) and cross section (right) of the first layers. Reproduced from Ref. [105].

2.2.2 CO and oxygen on Pt(110)

In the following, the structure of the catalyst surface and its interactions with the two reactants are briefly summarized. The adsorption and desorption kinetics for both CO and oxygen on platinum have been studied in great detail. In this section, only the main aspects of these processes are recalled. For a thorough discussion see Ref. [47] and for a survey of the literature relevant in the context of oscillatory kinetics Ref. [104].

Pt(110) Platinum shows a face centered cubic (fcc) crystal structure with a lattice parameter of $a = 3.92$ Å and a next neighbor distance between the platinum atoms of $d = 2.77$ Å. Here, we focus on the properties of the Pt(110) plane. In the non-reconstructed form, also denoted as the (1×1) structure, the Pt atoms on the (110) facet are arranged according to their bulk positions, see Fig. 2.5. However, the clean Pt(110) surface is known to undergo a reconstruction that leads to a corrugated surface structure composed of alternating rows and troughs of Pt atoms in the $[1\bar{1}0]$ direction as shown in Fig. 2.6 [106–110]. The reconstructed surface is characterized by a (1×2) LEED pattern and is commonly called the "missing row" structure. Compared to the particularly open structure of the (1×1) surface, the missing row structure contains a large fraction of energetically preferred (111) microfacets.

CO on Pt(110) Adsorption of CO on platinum takes place in molecular form. The initial sticking probability of CO on the (1×2) phase of the Pt(110) surface, s^0_{CO}, is close to unity [106, 111, 112]. Adsorption occurs via a precursor state, in which the CO

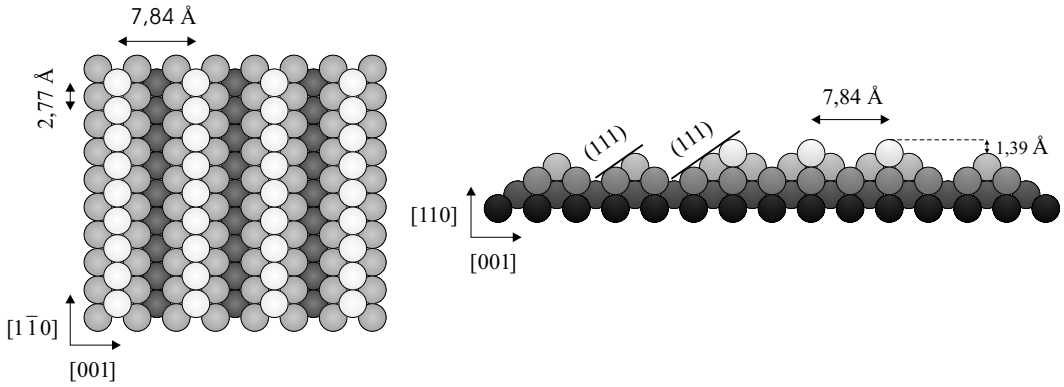

Figure 2.6: Hard-sphere model showing the (1×2) structure of the Pt(110) surface. Top view (left) and cross section (right) of the first layers. Reproduced from Ref. [105].

molecule is weakly bound to the metal surface and reaches its final adsorption site only after a hopping process between different sites. Therefore, the sticking coefficient remains almost constant for low coverages with CO. However, for higher coverages exceeding $u \approx 0.35$, it starts to decrease [106, 113]. Following Gasser and Smith [114], the precursor effect can be described according to $s_{\mathrm{CO}} = s^0_{\mathrm{CO}}\,(1 - u^q)$, with a mobility parameter q between 3 and 4. The saturation coverage with CO is equal to unity [106, 111, 115, 116].

The adsorption of CO on Pt(110) induces a structural change of the crystal surface [117]. The (1×2) missing row reconstruction of the clean platinum surface is lifted to the (1×1) bulk truncated phase. The transformation process starts with a CO coverage of 0.2 ML and is completed for a coverage of 0.5 ML [118]. At room temperature, it was shown that the transition is initiated by the appearance of uniformly distributed small patches of the (1×1) phase, formed by migration of Pt atoms over only a few lattice sites. At elevated temperatures, longer strings of Pt atoms are shifted in the [001] direction by quasi-correlated motion of adjacent atoms, so that larger domains of the (1×1) phase are formed [119].

CO is diffusively mobile on the Pt(110) surface. In general, CO diffuses more rapidly on the missing row surface than on the bulk terminated phase. However, due to anisotropy of the surface structure, the value of the diffusion constant depends on the crystallographic orientation. On both the (1×1) and the (1×2) phase, the diffusion constant is larger in the $[1\bar{1}0]$ direction compared to the [001] orientation [120].

Depending on the coverage, the thermal desorption spectra of CO show different shapes. For coverages below 0.4 ML a single peak is measured between 510 and 530 K. Up to a coverage of 0.5 ML, this peak shifts slightly towards lower temperatures and then remains at a constant position. Besides, a second peak appears for higher coverages at temperatures between 400 and 425 K, shifting to lower temperatures for increasing coverage. For a discussion, see Refs. [111, 113, 117].

Oxygen on Pt(110) At temperatures above 240 K, adsorption of oxygen takes place dissociatively following a second order kinetics with respect to the free adsorption sites [121]. At room temperature, the initial sticking probability for oxygen on the (1×2) surface of the Pt(110) facet is about 0.4 [122–124]. With growing oxygen coverage, the sticking coefficient decreases to 0.03 for a coverage greater than 0.35 ML [125]. On the (1×1) surface, the sticking coefficient is about 1.5 times higher for similar coverages [104, 124]. Also for oxygen adsorption, a precursor mediated mechanism has been proposed and the coverage dependence of the sticking coefficient can be fitted using a Kisliuk-type model [125]. Values for the saturation coverage have been determined between 0.3 and 0.35 ML [123, 124] for the (1×2) structure and at 0.8 for the (1×1) phase [124]. In a more recent work, however, a much higher coverage of 0.75 ML was measured also for the (1×2) surface [125].

Unlike the adsorption of CO, oxygen adsorption does not induce a lifting of the (1×2) reconstruction of the platinum surface [124, 126]. Also, the diffusive mobility of oxygen along the metal surface is different from diffusion of CO [120]. The activation energies for oxygen diffusion are much higher and the dependence on the crystallographic orientation is drastically increased. Diffusion of oxygen is practically limited to the $[1\bar{1}0]$ direction and no transport occurs perpendicular to the ridges of the missing row structure. Besides, a pronounced coverage dependence for the diffusion constant of oxygen was reported [120]. The experiments of the present work were performed in a temperature range between 450 and 550 K, where diffusion of oxygen can be neglected.

Oxygen desorbs only in molecular form. For low coverage, the thermal desorption spectrum shows a single peak around 830 K. With increasing coverage, the maximum is shifted towards lower temperatures as expected for second order desorption. However, for high coverages, desorption is described by a first order process and takes place at 740 K [121, 125].

2.2.3 Mechanism of the reaction

After having discussed the interactions of both CO and oxygen with the Pt(110) surface separately, we now turn to the reaction of the two components on the platinum surface. The catalytic oxidation of CO on platinum proceeds via a Langmuir-Hinshelwood mechanism [47]. Before the reaction can take place, both CO and oxygen have to adsorb from the gas phase on the catalytic surface. At temperatures considered in this work, desorption of CO has to be taken into account, whereas oxygen desorption can be neglected. An adsorbed CO molecule can react with an adsorbed oxygen atom from a neighboring lattice site to form carbon dioxide which is immediately released into the gas phase, leaving two vacant sites for adsorption of new educts. The reaction can be summarized in the following scheme,

$$\begin{aligned} 2\,\mathrm{CO} + 2\otimes &\rightleftharpoons 2\,\mathrm{CO}_{ad} \\ \mathrm{O}_2 + 2\otimes &\longrightarrow 2\,\mathrm{O}_{ad} \\ 2\,\mathrm{CO}_{ad} + 2\,\mathrm{O}_{ad} &\longrightarrow 2\,\mathrm{CO}_2\uparrow + 4\otimes, \end{aligned} \tag{2.6}$$

where $\otimes$ stands for a free adsorption site and the index '*ad*' denotes adsorbed molecules or atoms. In the following, some features of this mechanism are described that are of particular importance for the rich dynamical behavior of the reaction.

If both reactants are present in the gas phase they compete for empty adsorption sites on the catalyst surface. For several reasons, CO is in a more favorable position. While the dissociative adsorption of oxygen requires two adjacent free adsorption sites, a single empty site is sufficient for adsorption of a CO molecule. Besides, a weakly bound precursor state during CO adsorption allows hopping of the CO molecule between different locations so that binding to an adequate adsorption site becomes more likely. For the temperatures considered here, no similar mobility for oxygen is observed. Finally, the oxygen adsorbate layer exhibits an open structure with empty sites in between, always allowing the adsorption of additional CO. On the other hand, CO forms a compact adsorbate, completely covering and thus *poisoning* the catalyst surface against additional adsorption of oxygen so that no reaction can take place. This behavior is

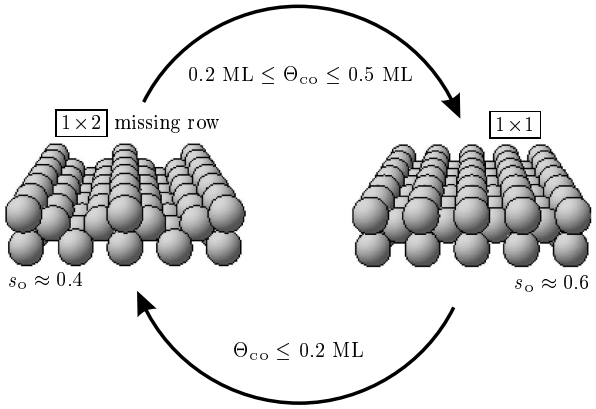

Figure 2.7: Schematic illustration of the adsorbate induced structural transition of the Pt(110) surface.

generally referred to as *asymmetric inhibition* and induces bistable dynamics in a wide range of parameters, where a mainly oxygen covered reactive state coexists with a CO covered non-reactive state.

Moreover, the system comprises an internal negative feedback loop, which is an essential prerequisite for excitable and oscillatory dynamics. This loop is established by the structural transition of the Pt(110) surface between the (1×2) missing row phase and the (1×1) bulk terminated structure. As described above, the sticking coefficient of oxygen is higher on the (1×1) structure as compared to the (1×2) surface. For an appropriate choice of parameters, adsorption of CO will dominate on the (1×2) surface, eventually inducing a lifting of the reconstruction to the (1×1) structure. On the (1×1) surface, however, the sticking probability of oxygen is increased leading now to a preferred adsorption of oxygen and, consequently, to an enhanced consumption of adsorbed CO due to reaction. If the CO coverage has dropped below 0.5 ML, the surface starts to reconstruct until the (1×2) missing row structure is reestablished at CO coverages below 0.2 ML. Now, the sticking probability for oxygen is reduced again and the process can start all over, see Fig. 2.7 [45].

Besides the $(1\times2) \leftrightarrow (1\times1)$ structural transition, a different microscopic restructuring process of the catalyst surface was observed. At temperatures below 530 K and under the influence of the catalytic reaction, the initially flat Pt(110) surface undergoes faceting into new orientations [127]. The characteristic size of the microfacets is about 100 Å and their formation occurs on a time scale of tens of minutes. Faceting of the Pt(110) plane is associated with an increasing catalytic activity and may lead to an induction period in the development of rate oscillations in catalytic CO oxidation [128].

Under certain conditions, the formation of an additional oxygen species could be observed [129]. Adsorbed oxygen was found to migrate underneath the top layer of the platinum surface upon an increase of temperature to form subsurface oxygen [130]. The subsurface oxygen can be released back onto the surface thus influencing the formation of concentration patterns on the catalyst. Detailed studies were performed for the Pt(100) [130, 131] and later the Pt(110) surface [132–134].

Two different mechanisms establish spatial coupling between the different locations on the catalyst surface. On the one hand, CO is diffusively mobile along the platinum surface as described in the previous section, providing local coupling between neighboring sites on the surface. On the other hand, global coupling through the gas phase is known to affect the dynamics of CO oxidation on Pt(110) significantly [135]. In the present work, only low pressure conditions are considered. In this regime, the mean free path of gas molecules is large compared to the dimensions of the vacuum vessel. Therefore, small changes in partial pressure induced by local consumption of educts from the gas phase will spread instantaneously throughout the system establishing a global coupling that equally acts on all parts of the system. The synchronizing effect of global gas phase coupling [136] and its impact on the formation of spatiotemporal patterns like standing waves [46] or oscillating cellular structures [137] were discussed in detail. A additional coupling may occur through the transport of heat in the catalyst. However, under low pressures, the heat production of the reaction can be neglected, so that isothermal conditions prevail and heat transport is absent. Only for higher pressures [97, 138] or ultrathin catalysts [139] the effects of thermal coupling become important.

2.2.4 Mathematical modeling

A simple mathematical model for the catalytic oxidation of CO on Pt(110) has been developed by Krischer, Eiswirth, and Ertl (KEE model) [48, 140]. Depending on the choice of external parameters, the model not only shows monostable and bistable behavior but also excitable and oscillatory dynamics. The bifurcation diagram of the homogeneous system has been analyzed in great detail [48, 104] and diffusive coupling was introduced to model the behavior of the spatially extended system [141]. The KEE model is well established and has been used for over a decade to study the dynamics

of catalytic CO oxidation on Pt(110) numerically. Many experimental observations of spatiotemporal pattern formation in the CO oxidation system could be reproduced, at least to a qualitative degree, in numerical simulations of the KEE model.

The KEE model The model consists of three coupled ordinary differential equations for the local dynamics, taking into account the most significant physical processes described in the previous section,

$$\partial_t u = k_1\, s_{\mathrm{CO}}\, p_{\mathrm{CO}} - k_2\, u - k_3\, uv\,, \tag{2.7}$$

$$\partial_t v = k_4\, s_{\mathrm{O}}\, p_{\mathrm{O_2}} - k_3\, uv\,, \tag{2.8}$$

$$\partial_t w = k_5\, [f(u) - w\,]\ . \tag{2.9}$$

The three variables u, v, and w are normalized between zero and one. They denote the CO coverage, the oxygen coverage, and the local fraction of the surface found in the nonreconstructed (1×1) structure, respectively. The system of Eqs. (2.7) – (2.9) can be regarded as a specific example of a dynamical system of type (2.1).

Both CO_{ad} and O_{ad} are consumed by reaction to carbon dioxide, proceeding with a rate constant of k_3 and taken into account by the last term in the Eqs. (2.7) and (2.8). In addition, the coverage with CO is reduced due to desorption with a rate constant of k_2, while oxygen desorption can be neglected at temperatures relevant in the context of this work. The adsorption processes of CO and oxygen are determined by the respective impingement rates k_1 and k_4, the sticking coefficients s_{CO} and s_{O}, and the partial pressures p_{CO} and $p_{\mathrm{O_2}}$ of the two components, respectively. As pointed out above, the sticking coefficients are coverage dependent. For s_{CO} a precursor effect has to be considered and is modeled following Gasser and Smith [114]. In the case of oxygen sticking s_{O}, a second order kinetics in the fraction of free sites is assumed and the difference in sticking probability between the (1×1) and (1×2) surface structures has to be accounted for. We thus obtain

$$s_{\mathrm{CO}} = s^0_{\mathrm{CO}}\,(1-u^3)\,, \tag{2.10}$$

$$s_{\mathrm{O}} = [\,s^0_{\mathrm{O},1\times1}w + s^0_{\mathrm{O},1\times2}(1-w)]\,(1-u-v)^2\,, \tag{2.11}$$

where s^0_{CO} and $s^0_{\mathrm{O},1\times1}$, $s^0_{\mathrm{O},1\times2}$ denote the initial sticking probabilities of CO and oxygen on the clean surface, respectively.

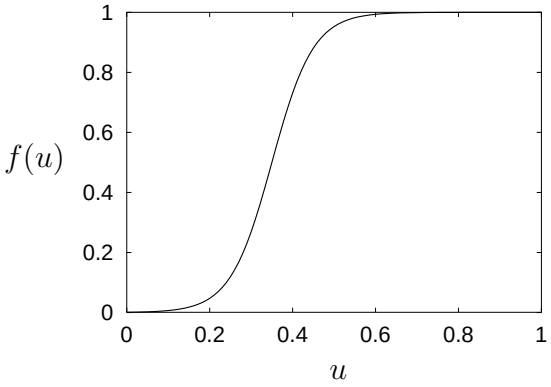

Figure 2.8: Plot of function $f(u)$ with $u_0 = 0.35$ and $\delta u = 0.05$, cf. Eq. (2.12).

Equation (2.9) describes the coverage dependent transition between the (1×2) missing row structure and the (1×1) bulk terminated surface taking place with a rate constant of k_5. While adsorption of CO induces a lifting of the (1×2) reconstruction, no such effect is observed for oxygen adsorption. Therefore, the function f, describing the equilibrium value of w in Eq. (2.9), is exclusively determined by u. In the original form of the KEE model [48], a piecewise approximation of f was used. Here, we use a different ansatz that was proposed later [132] and is computationally more convenient to handle while showing only small deviations from the piecewise approximation,

$$f(u) = \frac{1}{1 + \exp\left(\frac{u_0 - u}{\delta u}\right)} \,. \tag{2.12}$$

The parameters u_0 and δu determine the threshold above which the surface structure is significantly affected by the CO coverage and the steepness of the threshold, respectively.

The model shows three external control parameters that can be changed at will, namely the partial pressures p_{CO} and $p_{\mathrm{O_2}}$ of the two reactants and temperature. The rate constants k_2, k_3, and k_5 show a significant temperature dependence that is generally modeled assuming a simple Arrhenius-type relation,

$$k_i = \nu_i \exp\left(\frac{-E_i}{kT}\right) \,. \tag{2.13}$$

The reaction specific parameters such as sticking coefficients or activation energies were taken from the literature or determined in experimental studies of the individual reaction steps, see Refs. [48, 104, 142] and references therein.

The model Eqs. (2.7) – (2.9) describe the local dynamics of a single surface element without taking into account any spatial degrees of freedom (homogeneous dynamics, cf. Section 2.1.1). By introducing a spatial dependence of the variables u, v, and w, the dynamics on an extended single crystal surface can be modeled. Since diffusion of oxygen can be neglected at the temperatures considered here, local coupling between the different locations on the platinum surface is only established by diffusion of CO. Adding a respective diffusion term to Eq. (2.7) [49, 141, 143], the KEE model becomes an example of a spatially extended dynamical system of type (2.5).

Modifications The KEE model was changed and modified in many ways. A reduced two-variable version of the model was derived that gives qualitatively similar results for many aspects of the spatiotemporal dynamics [49, 144]. Spiral waves [145, 146] and the emergence of chemical turbulence in the excitable regime [85, 147] were successfully studied using the two-variable version.

Furthermore, the three-variable model has been extended to account for additional phenomena that were neglected in the original version. An important effect is the presence of global coupling through the gas phase as explained in the previous section. The model has been extended by an additional equation accounting for the evolution of CO partial pressure in the reaction chamber. In numerical simulations of the extended model, global coupling was found to influence the spatiotemporal dynamics significantly, inducing *e.g.* standing waves and cluster patterns [134, 148–153]. Other extensions of the three-variable version were proposed taking into account the influence of subsurface oxygen [132–134], or the overall effect of faceting of the single crystal surface on the dynamics [48].

2.2.5 Experimental setup

In this section, the laboratory setup for the experimental part of this work is briefly introduced. In particular, the photoemission electron microscope (PEEM) is described that was used to obtain spatially resolved images of adsorbate patterns on the catalyst.

UHV system The experimental studies of CO oxidation presented below were carried out in a stainless steel ultrahigh vacuum (UHV) chamber with a volume of about 60 L that is kept at a base pressure of approximately 10^{-10} mbar. The vacuum is maintained by a combination of two rotary vane pumps and three turbomolecular pumps. The rotary vane pumps are connected via zeolite traps to prevent contamination of the chamber by their lubricating oil. They establish a pressure of 10^{-3} mbar which serves as a fore-vacuum for the turbomolecular pumps used for evacuating the chamber. A titanium sublimation pump further improves the vacuum. The pressure inside the chamber is measured using an ionization manometer at low pressures and a baratron differential capacitance manometer under reaction conditions.

The chamber is equipped with standard instruments for surface studies under UHV conditions like low-energy electron diffraction (LEED) and Auger electron spectroscopy (AES). A differentially pumped quadrupole mass spectrometer (QMS) is used for detection of the different chemical species and for measuring of their partial pressures. The photoemission electron microscope (PEEM) is also operated under differential pumping. It is employed for imaging of concentration patterns on the crystal surface and will be described in more detail below.

The circular Pt(110) single crystal sample has a diameter of about 10 mm and is fixed inside the chamber to a sample manipulator that allows controlled movement of the sample in x-, y-, and z-direction as well as radial and azimuthal rotation by electric step

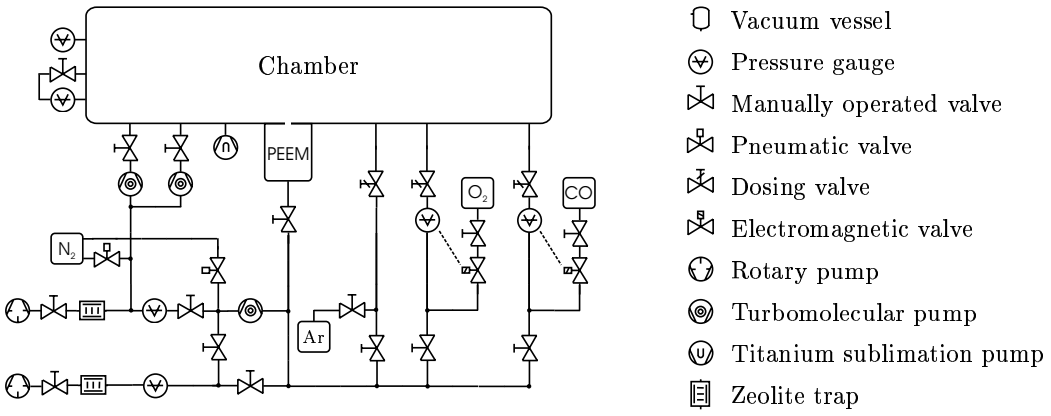

Figure 2.9: Schematic drawing of the UHV chamber with pumping and gas supply system. Reproduced from Ref. [105].

motors. Two different samples were used. The experiments presented in Chapters 3.2, and 4 were carried out on a Pt(110) crystal that was covered to approximately 80% by microlithographic deposition with Ti, leaving a number of small (about 1 mm^2 in size) isolated active Pt areas uncovered. Ti is easily oxidized to TiO_2, which is catalytically inert in the present reaction. In this way, the effects of intrinsic global gas phase coupling could be reduced. For experiments in the excitable regime (Chapter 6), a plain Pt(110) crystal was used. Sample heating was achieved by a halogen projector lamp mounted inside the sample holder directly behind the crystal. Prior to each experiment, the single crystal surface was prepared by repeated cycles of argon ion sputtering below 470 K, oxygen treatment at 570 K, and subsequent annealing up to 1000 K. Only purified gases were used for sample preparation and experiments (Ar 5.0, CO 4.7, and O_2 5.6). They were supplied by manually operated leak valves. To ensure stable partial pressures in the chamber, the supply of the reactants was additionally manipulated via electromagnetic valves that were automatically controlled by an electronic feedback system. During experiments, gases were constantly supplied and pumped so that the chamber was operated as a continuous flow reactor. For more details on the UHV system see Ref. [154].

Photoemission electron microscope In this work, spatiotemporal pattern formation during CO oxidation on Pt(110) was experimentally studied by means of photoemission electron microscopy (PEEM). Since 1990, photoemission electron microscopy is used for imaging of adsorbate patterns on catalytic surfaces [46, 96, 155, 156]. The PEEM yields spatially resolved information on the local work function across the sample surface. Due to the adsorbate dependence of the work function, different values of work function can be translated into adsorbate coverages so that images of lateral concentration distributions on the catalyst surface become accessible in real time. For a review the reader is referred to [94, 157].

To induce the emission of photoelectrons, the platinum sample is irradiated with ultraviolet light from a 200 W deuterium discharge lamp. Under air, the spectrum of the lamp is limited towards high energies at around 6.8 eV due to absorption of oxygen. In the platinum CO oxidation system, this causes large variations in the photoelectron yield because here the Pt surface shows a work function φ between 5.5 and 6.5 eV depending on the adsorbate coverage. To capture as many photoelectrons for the imaging

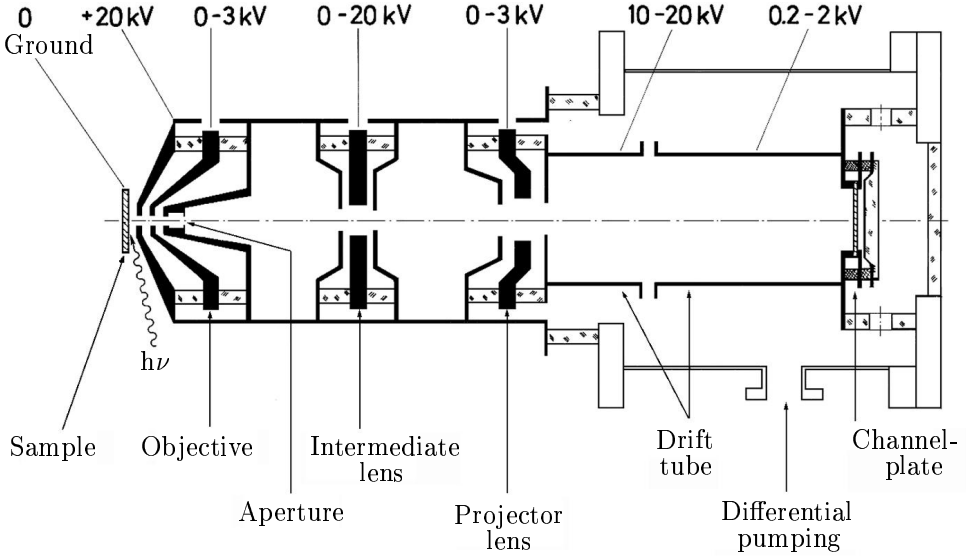

Figure 2.10: Schematic drawing of the photoemission electron microscope (PEEM). Reproduced from Ref. [155].

as possible, the objective of the PEEM is mounted in a distance of about 4 mm closely in front of the sample. In addition, the electrons are accelerated in a potential difference of 20 kV between sample and front opening of the PEEM. The distribution of electrons is then imaged by a system of three electrostatic lenses onto a channelplate with a diameter of 4 cm [155]. Here, the local electron signal is amplified by a factor of 10^3. A phosphor screen converts the electron distribution into a light intensity image which is then recorded by a CCD camera at a frame rate of 25 images per second.

The clean Pt surface has the lowest work function φ and, therefore, displays the brightest image intensity. The work function of the CO-covered surface is slightly increased compared to the clean surface ($\Delta\varphi = +0.3$ eV) causing a small decrease in the yield of photoelectrons and hence in the intensity of the PEEM image compared to the clean surface. Finally, O-covered areas appear nearly dark due to a more pronounced increase of the work function ($\Delta\varphi = +0.8$ eV). In the experiments presented here, the imaged area on the sample surface is typically of a diameter of $500\,\mu$m with a spatial resolution of $1\,\mu$m.

2.3 Electrochemical oxidation of hydrogen on Pt

Apart from heterogeneous catalytic reactions, there are many other chemical processes that display spatiotemporal self-organization. There is, in particular, a large number of electrochemical systems showing instabilities and complex space-time behavior. For a review of nonlinear phenomena in electrochemical systems see Refs. [10, 158].

In this section, the electrochemical oxidation of hydrogen is introduced as an example of an electrochemical system with rich spatiotemporal dynamics. It complements the CO oxidation system in several aspects as a model system for the experimental study of pattern formation. In the present setup, the space-time behavior of electrochemical hydrogen oxidation is investigated along a ring electrode. As the width of the electrode is small compared to its circumference, a quasi-one-dimensional system with periodic boundary conditions is realized. This allows to contrast the results from the two-dimensional CO oxidation system with the dynamical behavior in one spatial dimension. Besides, in this type of system, diffusive transport can be neglected and spatial coupling is established by migration instead. The range of migration coupling in electrochemical systems can be controlled by changing the geometry of the electrochemical cell allowing to study the spatiotemporal behavior for different coupling ranges.

2.3.1 General remarks

In the following, a few selected general aspects of electrochemical systems are recalled, as far as they are essential for the subsequent discussion. A comprehensive introduction to the subject can be found in standard electrochemistry textbooks, *e.g.* in Refs. [159, 160].

In Fig. 2.11 (a), the schematic view of an electrochemical setup is displayed. A voltage U is applied between working electrode (WE) and reference electrode (RE), the total current I flowing between working and counter electrode (CE). Both potentiostatic or galvanostatic control can be established in this setting maintaining constant U or I, respectively. At the electrode-electrolyte interface, charge distributions reorganize and

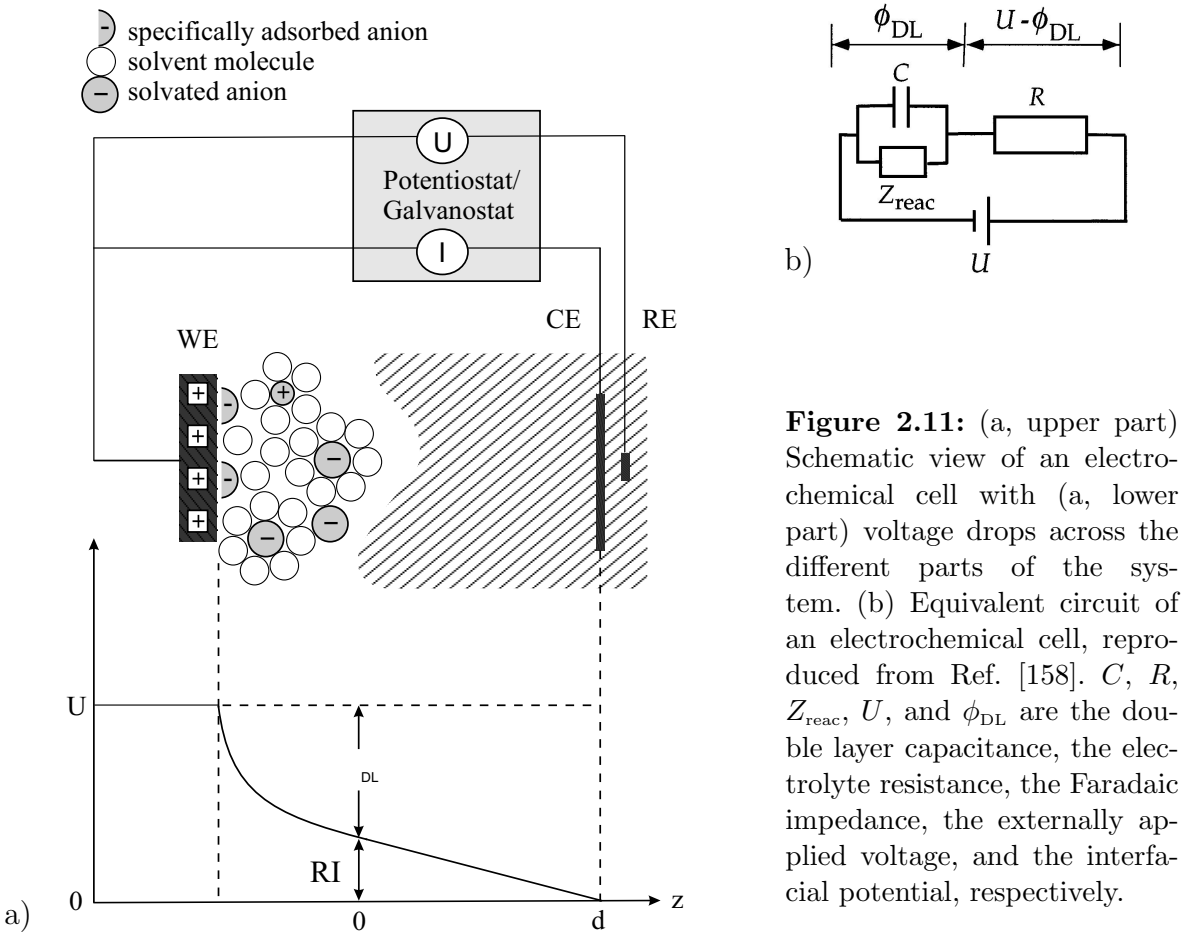

Figure 2.11: (a, upper part) Schematic view of an electrochemical cell with (a, lower part) voltage drops across the different parts of the system. (b) Equivalent circuit of an electrochemical cell, reproduced from Ref. [158]. C, R, Z_{reac}, U, and ϕ_{DL} are the double layer capacitance, the electrolyte resistance, the Faradaic impedance, the externally applied voltage, and the interfacial potential, respectively.

an *electric double layer* may form that consists of hydrated ions accumulating in front of the electrode. They are compensated by equal counter charges in the metal. Although its detailed structure is complicated, it is sufficient to describe the double layer in this context as a capacitor characterized by the specific double layer capacitance C. The voltage drop across the double layer is denoted as the *double layer potential* ϕ_{DL}. It is the key quantity in most electrochemical processes and also the essential dynamical variable for nonlinear behavior of electrochemical systems. Taking into account the resistance R of the electrolyte, the total potential drop between WE and RE is

$$U = \phi_{\mathrm{DL}} + IR\,, \tag{2.14}$$

with I denoting the current flowing through the cell. An equation for the temporal dynamics of the double layer potential can be derived considering the standard equivalent

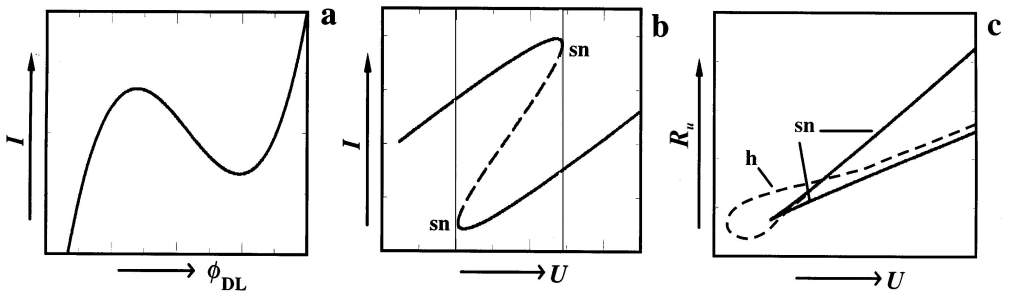

Figure 2.12: N-NDR system. (a) Negative differential resistance due to an N-shaped current-potential characteristic. (b) Bistability in current vs. external voltage curve, sn denoting the saddle node bifurcations. (c) Bifurcation diagram in the parameter plane spanned by the external voltage and the cell resistance. At the dashed line, a Hopf bifurcation to oscillatory behavior occurs. Reproduced from Ref. [158].

circuit of an electrochemical cell, see Fig. 2.11 (b). Current can pass the double layer on two routes: as a Faradaic current j_{reac} arising from charge transfer in an electrode reaction or as a capacitive current charging the double layer. The resistance R of the bulk electrolyte appears in series with the interface. Applying Kirchhoff's law and normalizing to unit electrode area, the temporal evolution of the double layer potential for a WE of area A is governed by

$$C\frac{\mathrm{d}\phi_{\mathrm{DL}}}{\mathrm{d}t} = -j_{\mathrm{reac}} + \frac{U-\phi_{\mathrm{DL}}}{R\,A}\,. \tag{2.15}$$

2.3.2 Reaction

Similar to self-organization in other extended nonequilibrium systems, spatiotemporal pattern formation in electrochemical systems can be explained as a combination of local dynamics and spatial coupling between the different locations in the system [158]. Here, the homogeneous dynamics of electrochemical hydrogen oxidation on Pt will be presented followed by a discussion of coupling mechanisms in the next section.

Most instabilities in electrochemical systems are related to a negative differential resistance (NDR) in the current-potential characteristic occurring in almost any electrochemical system for an appropriate choice of parameters. Two types of NDR may be distinguished. On the one hand, the current-potential curve can exhibit an N-shaped characteristic (N-NDR) as shown in Fig. 2.12 (a). This behavior is found in many elec-

trochemical systems. Although it may occur as the result of different physical processes, this feature can be modeled in most cases by assuming a third order polynomial dependence of the reaction current j_{reac} on the double layer potential ϕ_{DL}. With changing potential drop in the electrolyte, the polarization curve can change its shape, leading to bistability and oscillatory dynamics, see Fig. 2.12 (b), (c). In some of these systems, generally referred to as HN-NDR systems (hidden N-NDR), the N-shaped characteristic is hidden by another potential dependent process. Here, the NDR is observed only in a subsystem while the reaction for the full system is inhibited at the respective potential values. On the other hand, NDR is encountered in some systems displaying a S-shaped polarization curve (S-NDR). This case is considerably less frequent and behaves in many aspects complementary to the N-NDR situation.

The electrochemical oxidation of hydrogen on Pt is an example of a system with N-shaped polarization curve that can be turned into a HN-NDR system by addition of electrosorbing ions like Cl^- and Cu^{2+}. The anodic hydrogen oxidation proceeds through the following mechanism,

$$\begin{aligned} \mathrm{H_2^{bulk}} &\longrightarrow \mathrm{H_2^{surface}} \\ 2\,\mathrm{Pt} + \mathrm{H_2^{surface}} &\longrightarrow 2\,\mathrm{Pt\text{–}H} \\ \mathrm{Pt\text{–}H} + \mathrm{H_2O} &\longrightarrow \mathrm{H_3O^+} + \mathrm{e^-} + \mathrm{Pt}\,, \end{aligned} \tag{2.16}$$

accounting for hydrogen diffusion from the bulk electrolyte to the electrode surface, dissociative adsorption of hydrogen on the Pt electrode, and electrochemical oxidation of adsorbed hydrogen with subsequent hydration of the protons. For details on the electrocatalytic oxidation of hydrogen, see Ref. [161] for a recent review and references therein. With growing potential, formation of platinum oxide increasingly blocks free sites on the electrode surface leading to a decrease in current and hence to a NDR.

If Cl^- ions are present, they may adsorb on the electrode inducing an additional NDR at smaller potentials. In the same range, Cu^{2+} inhibits the reaction and desorbs only for increasing potential thus forming a prototypical HN-NDR type system. For an appropriate choice of parameters, the counteracting adsorption kinetics of these two additives lead to oscillatory behavior of the reaction, see *e.g.* Refs. [162, 163].

2.3.3 Migration coupling

Different mechanisms may introduce spatial coupling between the individual locations on the electrode [10]. For instance, both galvanostatic and potentiostatic control of the experiment can *externally* impose a global coupling by making the local dynamics dependent on the average double layer potential. The basic mechanism that provides an *intrinsic* spatial coupling in electrochemical systems is due to migration and will be presented in the following.

As discussed in Section 2.3.1 above, current can pass the double layer on either the Faradaic or the capacitive pathway, cf. Fig. 2.11 (b). Complying with local charge balance at the interface, a change in the double layer potential has to be equal to the difference between the migration current flowing into the double layer and the Faradaic current density at each location. Thus, the spatiotemporal evolution of the double layer potential $\phi_{\mathrm{DL}}(x,t)$ can be written as

$$C\frac{\partial \phi_{\mathrm{DL}}}{\partial t} = -j_{\mathrm{reac}} - \sigma \frac{\partial \phi}{\partial z}\bigg|_{\mathrm{WE}}. \tag{2.17}$$

Here, the left hand side expresses the local charging of the interface with C the specific double layer capacitance. The local Faradaic current density is denoted by j_{reac}. The migration current density is proportional to the normal derivative of the electric potential in the electrolyte ϕ at the position of the working electrode (WE) with σ the specific conductivity of the electrolyte.

Spatial coupling is established through the last term in Eq. (2.17). Assuming a uniform distribution of concentrations, the electric potential ϕ in the bulk electrolyte can be determined by solving Laplace's equation. Since the solution depends on boundary conditions, the geometry of the system plays a crucial role. In a two-dimensional arrangement, as is sufficient to consider here, the distance d between WE and CE is the important geometric parameter. Note that in the present arrangement, where the RE is located behind the CE, also the potential drop between WE and RE is determined by d, since there is effectively no current flowing beyond the CE. Moreover, with the WE being one of the boundaries, local changes in the double layer potential affect the potential distribution in the whole electrolyte. They are felt instantaneously all over

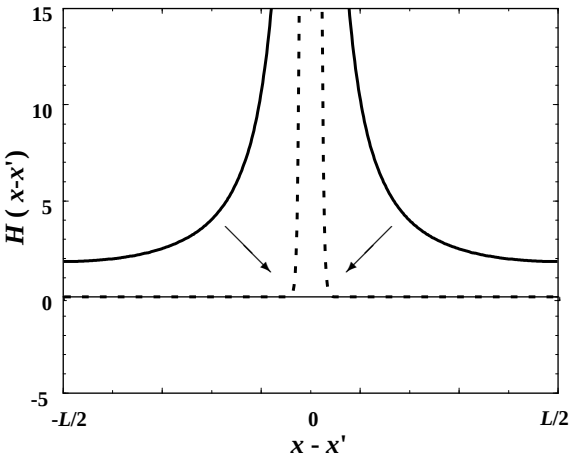

Figure 2.13: Coupling function H of a ring electrode for nonlocal migration coupling (solid line). With decreasing d, the coupling becomes more localized (arrows) and converges to the diffusive case in the limit $d \to 0$ (dashed line). The width of the ring is assumed to be small compared to the circumference L and the distance between WE and RE is larger than $2L$. The coordinate x denotes angular direction. Reproduced from Ref. [158].

the electrode and induce variations in the migration currents at all other locations on the electrode. Thus, migration coupling acts not only between next neighbors, but shows a long-range impact.

The contributions to the migration current that are actually due to lateral differences in the interfacial potential can be expressed by subtracting the current that is flowing in the case of a homogeneous potential distribution,

$$C\frac{\partial \phi_{\mathrm{DL}}}{\partial t} = f - \sigma\left[\left.\frac{\partial \phi}{\partial z}\right|_{\mathrm{WE}} + \left(\frac{U-\phi_{\mathrm{DL}}}{d}\right)\right], \tag{2.18}$$

where $f = -j_{\mathrm{reac}} + \sigma(U-\phi_{\mathrm{DL}})/d$. This equation shows an analogy to reaction-diffusion systems (2.5) in the sense that the first term on the right hand side represents the dynamics of the uniform system, while the second term accounts for coupling due to local differences in the dynamic variable.

Similar to diffusion, migration coupling acts synchronizingly. However, as outlined above, it is mediated through the electric potential ϕ in the electrolyte and therefore can show a long-range effect. The range of migration coupling depends on the distance d between WE and CE. For large d, the coupling is nonlocal. A localized perturbations in the interfacial potential leads to a reorganization of the electric potential ϕ in the electrolyte. The impact of such a perturbation is felt not only in z-direction but also spreads in x-direction and affects more remote positions on the ring. For smaller d, the spread in x-direction becomes less, so that the coupling is more localized and converges to diffusive coupling in the limit $d \to 0$. The nonlocal character of migration

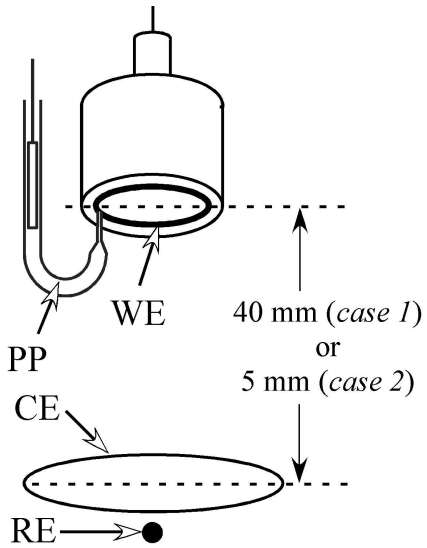

Figure 2.14: Experimental setup [165]: Ring shaped working electrode (WE) and counter electrode (CE), reference electrode (RE, Hg/Hg_2SO_4 saturated) located below the plane of the CE. The WE is rotated with 20 Hz and the spatial distribution of the interfacial potential is sampled by a potential probe (PP) with a resolution of 50 points per rotation. The two different separations of WE and CE refer to the different cases presented in Section 3.1.

coupling becomes more obvious when transforming the last term of Eq. (2.18) into a more intuitive integral formulation as demonstrated by Christoph *et. al.* [164],

$$-\sigma\left[\left.\frac{\partial\phi}{\partial z}\right|_{\mathrm{WE}}+\left(\frac{U-\phi_{\mathrm{DL}}}{d}\right)\right]=\sigma\int_{\mathrm{WE}}H(|x-x'|)(\phi_{\mathrm{DL}}(x')-\phi_{\mathrm{DL}}(x))\,\mathrm{d}x\,. \tag{2.19}$$

For a ring electrode of circumference L, Fig. 2.13 displays the typical shape of the coupling function H for nonlocal migration coupling (solid line) and diffusion coupling (dashed line) in comparison.

2.3.4 Experimental setup

A schematic draft of the experimental setup is presented in Fig. 2.14. The ring shaped WE is made of polycrystalline Pt embedded in a cylindrical Teflon piece. It is 1 mm in width and has a mean circumference of 85 mm. The local electric potential in the electrolyte close to the WE is recorded using a stationary potential probe. By rotating the WE over the potential probe, the temporal evolution of the angular potential distribution in front of the Pt ring can be obtained *in situ*. Besides, the rotation of the ring ensures a defined mass transport of H_2 as well as Cu^{2+} and Cl^- ions from the bulk electrolyte to the reaction plane at the WE. To establish radial symmetry in the electrochemical cell, also the Pt counter electrode was ring shaped. For further details on the experimental setup see Refs. [166–168].

2.4 General models

In the last part of this chapter, general models are introduced that describe common aspects of extended oscillatory systems. Throughout this work, the results from specific experimental systems, in particular from catalytic CO oxidation, will be discussed in comparison to theoretical predictions from these simplified universal descriptions. In this way, it is possible to evaluate the relevance of experimental observations from a specific system for the class of oscillatory systems at large.

2.4.1 The complex Ginzburg-Landau equation

The complex Ginzburg-Landau equation (CGLE) is one of the most thoroughly studied nonlinear equations in physics. For a detailed discussion and a recent review, see Ref. [169] and references therein. In the following section, only a few introductory remarks to the CGLE are presented and its basic properties are briefly reviewed with some emphasis on spatiotemporal chaos.

General remarks The individual properties of a dynamical system (2.5) can be complex and may differ strongly from one system to another. However, close to a bifurcation point, the description of such systems can be simplified considerably. In general, instabilities in extended systems are classified by analyzing the response behavior to single Fourier mode perturbations. By linearizing around a uniform steady state, the evolution of modes $u_j(x,t) = u_{j0}\, e^{iqx+\lambda t}$ is studied, focusing on the most unstable mode (the mode for which $\mathrm{Re}(\lambda)$ is largest). Near the bifurcation point, $\mathrm{Re}(\lambda)$ is close to zero for these modes. Thus, their evolution becomes slow compared to the remaining stable modes. Due to this separation of time scales in the vicinity of a bifurcation point, the dynamics of a large number of stable modes relaxes to the evolution of a few leading critical modes. Their behavior is 'enslaved' to the evolution of the most unstable modes so that they may be eliminated adiabatically. In this way, the system of Eqs. (2.5) can be reduced to a simple *amplitude equation* for the critical modes that captures the dynamics of the full system close to the bifurcation point. The form of the amplitude equation depends on the type of instability and is *universally valid* for all systems showing this bifurcation. For amplitude equations in general, see *e.g.* Ref. [66].

With respect to oscillatory systems, the supercritical Hopf bifurcation is of particular interest as the most simple bifurcation leading to oscillatory dynamics, cf. Section 2.1.1. By the above arguments, the dynamics of any system showing this type of bifurcation can be described, in the immediate vicinity of the bifurcation point, by a universal equation. Retaining only the leading modes close to the Hopf point, the complex Ginzburg-Landau equation (CGLE) is obtained for an extended system of diffusively coupled elements. Because of its universal character, the CGLE can be considered as a model system for extended oscillatory systems in general. At the onset of periodic behavior in a supercritical Hopf bifurcation, oscillations have small amplitudes and are approximately harmonic. The CGLE describes these oscillations in terms of a complex variable $\eta = \rho\, e^{i\phi}$ with amplitude $\rho = |\eta|$ and phase $\phi = \arg(\eta)$. After appropriate scaling of the coefficients, the CGLE reads

$$\partial_t \eta = (1 - i\omega)\eta - (1 + i\beta)|\eta|^2\eta + (1 + i\varepsilon)\nabla^2\eta\,. \tag{2.20}$$

For details of the derivation of Eq. (2.20) from a full dynamical system of type (2.5), see *e.g.* Ref. [68]. The linear frequency parameter ω denotes the difference to the oscillation frequency at the Hopf point and can be eliminated by changing to a rotating coordinate frame, $\eta \to \eta\, e^{i\omega t}$. Thus, the dynamics of the CGLE effectively depends on the two real parameters β and ε, denoting a nonlinear frequency shift and a linear dispersion coefficient, respectively.

The values for β and ε can be determined for any specific reaction-diffusion system (2.5) close to a Hopf point. In this work, however, the CGLE coefficients are not derived from a realistic model and no quantitative comparison with experimental results is carried out. Instead, the CGLE will be considered as a general model for oscillatory systems and its behavior will be taken to complement observations from specific experimental systems with aspects common to all oscillatory media. Although strictly applicable only sufficiently close to the onset of oscillations, it was found in many cases that the predictions of the CGLE remain qualitatively valid in a wider distance from the bifurcation point. The dynamics of the CGLE shows a wealth of different spatiotemporal phenomena including the occurrence of plane waves and spiral waves as well as localized coherent structures and spatiotemporally chaotic regimes.

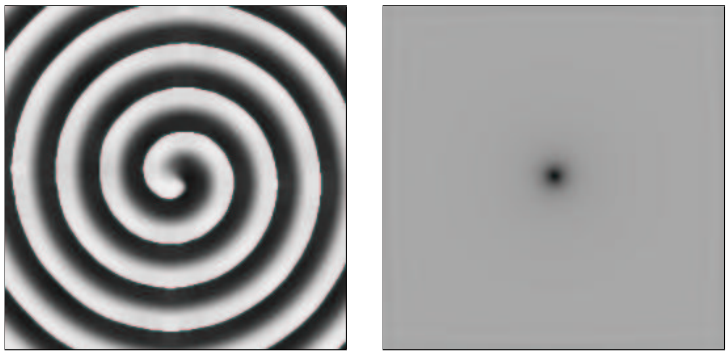

Figure 2.15: Spiral wave solution of the two-dimensional CGLE, reproduced from Ref. [171]. Phase (left) and amplitude (right) are displayed in gray scale. Dark (light) denote low (high) values.

Uniform oscillations If oscillations in the complex amplitude η are uniform throughout space, diffusive coupling can be neglected and the dynamics is effectively described by an ordinary differential equation for a single oscillator,

$$\partial_t \eta = (1 - i\omega)\eta - (1 + i\beta)|\eta|^2 \eta \,, \tag{2.21}$$

sometimes referred to as the *Stuart-Landau equation* (SLE). Obeying this equation, the complex amplitude performs stable limit cycle oscillations, $\eta = \rho_0 \, e^{-i\Omega t}$, with constant frequency and amplitude,

$$\Omega = \omega + \beta \qquad \text{and} \qquad \rho_0 = 1 \,. \tag{2.22}$$

In the spatially extended system (2.20), uniform oscillations are stable only if the condition $1 + \varepsilon\beta > 0$ is fulfilled. If the Newell criterion $1 + \varepsilon\beta < 0$ is satisfied, synchronous oscillations become linearly unstable. They undergo the *Benjamin-Feir instability* and turbulence spontaneously develops [170], see below.

Plane and spiral wave solutions The CGLE has a family of plane wave solutions,

$$\eta(x,t) = \rho_k \exp(ikx - i\omega_k t) \,, \tag{2.23}$$

with amplitude $\rho_k = \sqrt{1 - k^2}$ and frequency $\omega_k = \Omega + (\varepsilon - \beta)k^2$, where $\Omega = \omega + \beta$ denotes the frequency of uniform oscillations. The amplitude of plane waves converges to the amplitude of uniform oscillations in the long-wavelength limit ($k \to 0$) and vanishes as k approaches unity ($k \to 1$) not allowing a wavelength smaller than 2π. However, plane waves are only stable for wave numbers $k^2 < k_E^2$, where k_E is determined by the so-called *Eckhaus instability* [169].

Particularly well studied typical solutions of the CGLE in two spatial dimensions are spiral waves, see Fig. 2.15 for an example. In general, the complex amplitude of a spiral wave is described by

$$\eta(r,\theta,t) = \rho(r)\exp(-i\phi(r,\theta,t))\,, \tag{2.24}$$

where r, θ are polar coordinates in the two-dimensional plane. The phase ϕ of a spiral wave can be written as

$$\phi(r,\theta,t) = \omega t - m_{\text{top}}\theta - \psi(r)\,. \tag{2.25}$$

Here, ω, m_{top}, and ψ denote the frequency, the topological charge, and the radial phase contribution of the spiral wave, respectively. The topological charge takes the value $m_{\text{top}} = \pm 1$ for single-armed spirals, the direction of rotation depending on the sign of m_{top}. Along any closed contour around the center of such spiral waves, the phase changes by an amount of $\Delta\phi = \pm 2\pi$. The center itself constitutes a topological defect, where the real amplitude ρ vanishes and the phase is not defined. The total topological charge of a medium with periodic boundaries is conserved. Thus, topological defects can be only created and annihilated in pairs of opposite sign. Spiral waves may become unstable leading to spiral breakup that typically results in a spatiotemporally chaotic behavior [172]. Spiral breakup was also observed experimentally [67, 173] and in numerical simulations [174].

Turbulence In the Benjamin-Feir unstable regime, $1+\varepsilon\beta < 0$, uniform oscillations are unstable with respect to small perturbations and irregular, spatiotemporally chaotic states spontaneously develop in the system. These dynamical regimes are often referred to as *chemical turbulence* [68, 69].

For a one-dimensional system, the first systematic study was performed by Shraiman *et al.* [170]. Close to the Benjamin-Feir boundary, *phase turbulence* is observed. Here, the local oscillation phase exhibits weak irregular fluctuations. The real amplitude remains saturated and is characterized by randomly traveling shocks of increased oscillation amplitude. For space-time diagrams of both phase and amplitude, see Fig. 2.16 (a). In this regime, the system still shows long-range phase correlations. Farther away from the instability, *amplitude* or *defect turbulence* develops, characterized by strong fluctu-

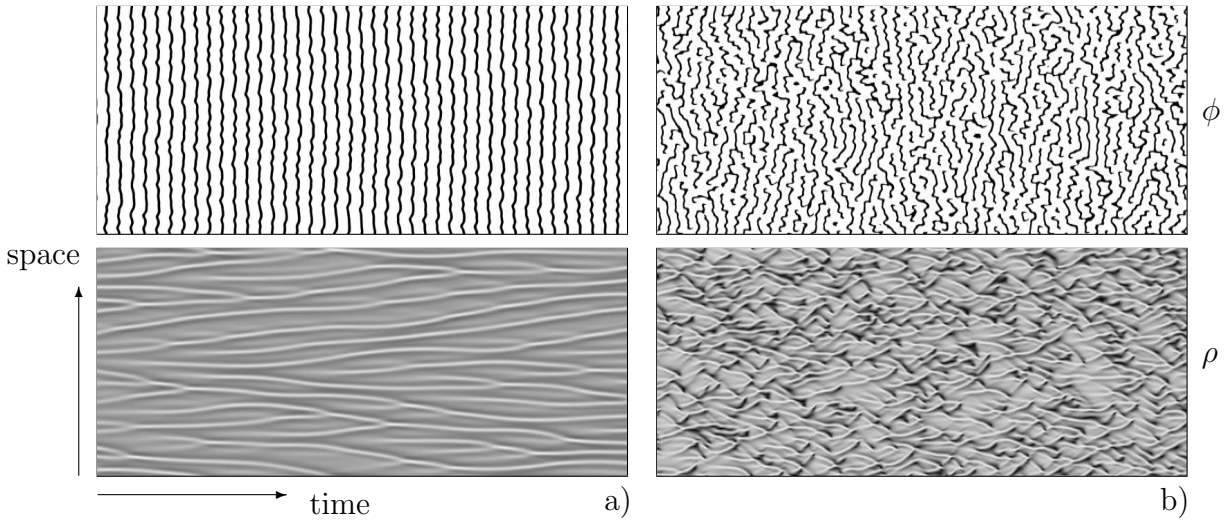

Figure 2.16: (a) Phase turbulence and (b) amplitude turbulence in the one-dimensional CGLE. (top) Space-time diagrams showing lines of constant phase ϕ and (bottom) the amplitude fields ρ in gray scale are displayed. Dark (light) denote low (high) values of the amplitude. Space-time defects occur at the end of constant phase lines. The system size is $L = 256$ and the displayed time interval is $\Delta t = 300$. The parameters are (a) $\beta = -0.91$, (b) $\beta = -1.4$, and $\varepsilon = 2$, $\omega = 0$ in both cases.

ations of both phase and real amplitude which are due to the presence of space-time defects — locations with vanishing real amplitude where abrupt changes in the phase occur (phase slips), see Fig. 2.16 (b). The transition from phase to amplitude turbulence is associated with a pronounced decrease in spatial correlation. It has been studied since the beginning of the 1990s [170, 175] and is a matter of ongoing debate [176, 177]. Depending on the choice of ε, the two turbulent regimes may be separated by a so-called "bichaotic" region, where both phase and amplitude turbulence can occur. Besides, defect chaos may even coexist with stable plane wave solutions in the Benjamin-Feir stable regime. In this range of *intermittent turbulence*, laminar patches of plane waves are typically separated by defects that are replicating in repeated cascades but do not invade the entire medium [178, 179].

The most detailed numerical studies of chaotic regimes in two dimensions were carried out by Chaté and Manneville [172, 180]. As in one spatial dimension, two types of turbulent behavior can be distinguished. Close to the instability, phase turbulence prevails, where phase correlations show a slow power-law decay. In this parameter range, disordered cellular structures are formed that slowly evolve in time, see snapshots

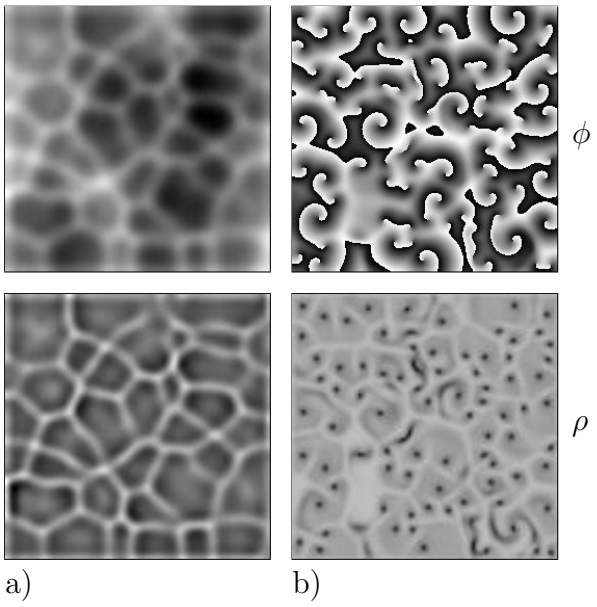

Figure 2.17: Snapshots of (a) phase turbulence and (b) amplitude turbulence in the two-dimensional CGLE, reproduced from Ref. [171]. (top) Phase ϕ and (bottom) amplitude ρ are displayed in gray scale. Dark (light) denote low (high) values.

in Fig. 2.17 (a). In the strongly irregular regime of amplitude turbulence, both spatial and temporal correlations decay exponentially with short correlation lengths and times. Amplitude turbulence in two dimensions is characterized by the presence of topological defects [181]. They are continuously created and annihilated, and their behavior can be described in terms of statistical properties [182]. A snapshot from a time series displaying amplitude turbulence is shown in Fig. 2.17 (b).

2.4.2 Phase dynamics approximation

Under certain conditions, the description of an oscillatory medium can be simplified even further to a reduced formulation in terms of a phase variable only [25, 68]. For a limit cycle oscillator amplitude, frequency, and orbital form of self-oscillations are specific features determined by the properties of the individual oscillator. The phase, however, remains arbitrary. Upon application of a small perturbation, the initial shape and amplitude of oscillations will be reestablished after a characteristic relaxation time τ_r. The phase, on the other hand, will not recover its initial value but will maintain a small shift induced by the perturbation. In an extended system of diffusively coupled limit cycle oscillators, the evolution of a spatial phase distribution will therefore depend on the length scale L of phase variations across the medium. If the phase distribution is sufficiently smooth, the characteristic time scale of its evolution will be large compared

to τ_r. In this case, the amplitude adjusts adiabatically to the local phase gradient and can be eliminated as an independent variable. This yields an effective equation for the dynamics of smooth phase distributions. It has the following universal form,

$$\partial_t \phi = a(\nabla\phi)^2 + b\nabla^2\phi\,, \tag{2.26}$$

and remains valid as long as the characteristic length scale L of the phase distribution fulfills $L \gg \sqrt{b\,\tau_r}$. The parameters a and b depend on the particular system. By use of the Hopf-Cole transformation, $\phi = (b/a)\ln Q$, Eq. (2.26) can be rewritten as a simple linear equation,

$$\partial_t Q = b\nabla^2 Q\,. \tag{2.27}$$

For positive b, Eq. (2.27) has the form of a standard diffusion equation. Here, localized perturbations in Q (and thus in ϕ) get smoothed out and oscillations will eventually become synchronized. On the other hand, if b is negative, spatial perturbations will grow in magnitude and get increasingly localized. In this case, uniform oscillations are linearly unstable. They undergo a Benjamin-Feir-type instability leading to an irregular spatiotemporally chaotic dynamical state. Note that in this regime, phase gradients become steeper in the course of time, so that the condition of sufficiently smooth phase variations gets violated and Eq. (2.26) is no longer valid. Therefore, a complete description of the turbulent regime can be given only in terms of the full set of equations of the dynamical system. However, close to the Benjamin-Feir line, it can be expected that the instability develops slowly and the system remains in the vicinity of uniform limit cycle oscillations. In this case, the emerging chaotic state of phase turbulence can still be described in terms of a phase dynamics approximation — the *Kuramoto-Sivashinsky equation* [68]. It is derived by an extension of Eq. (2.26) to higher-order terms in the spatial phase derivatives.